Supplementary information

Heterostructured electrode for Cr-tolerant solid oxide fuel cells

Sehee Bang[‡a], Jongseo Lee[‡b], Joon Gyu Kim[a], Jinwoo Kim[c], Mingi Choi[c], Yan Chen[d], Wonyoung Lee[a,e,*]

[a]School of Mechanical Engineering, Sungkyunkwan University, Suwon 16419, Republic of Korea

[b]Advanced Defense Science and Technology Research Institute, Agency for Defense Development, Daejeon 34186, South Korea

[c]Department of Future Energy Convergence, Seoul National University of Science & Technology, Seoul 01811, Republic of Korea
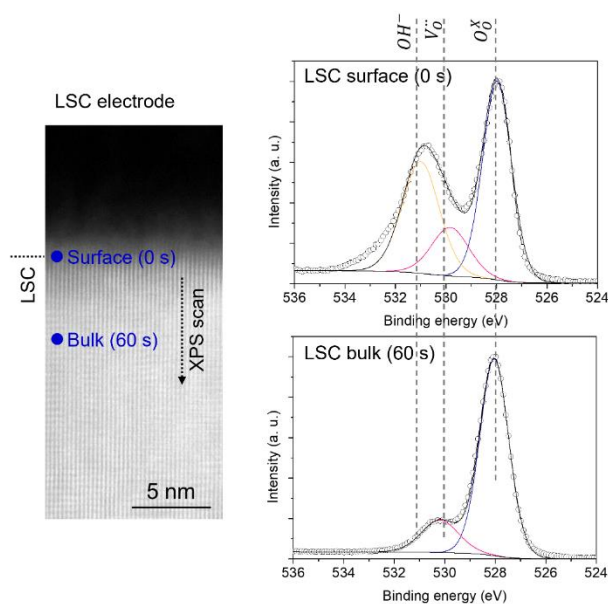
[d]School of Environmental and Energy, South China University, Guangzhou 510006, P. R. China

[e]SKKU Institute of Energy Science and Technology (SIEST), Sungkyunkwan University, Suwon 16419, Republic of Korea

*Corresponding author*: leewy@skku.edu (Wonyoung Lee)
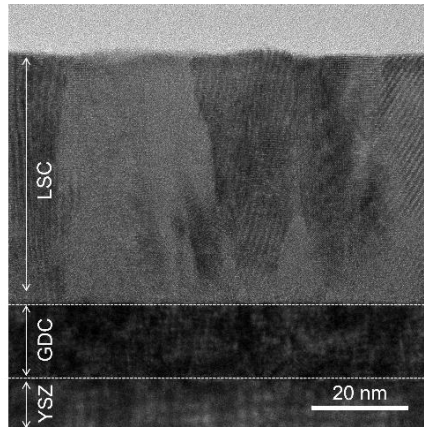
Figure S1. Cross-sectional TEM image of the as-deposited LSC electrode.
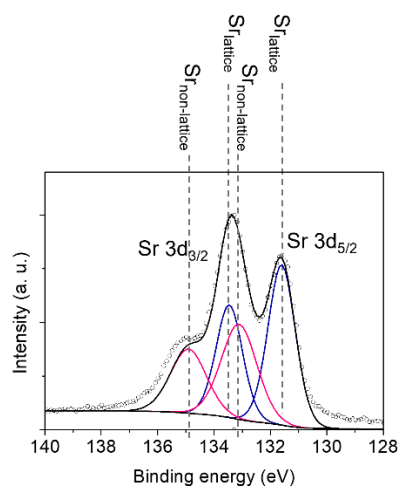
Figure S2. Fitting of the O 1s photoelectron spectra in the thickness direction.

O 1s photoelectron spectra were deconvoluted into three binding states: hydroxyl group (OH⁻, 531.2 eV), oxygen-related defects ($V_O^{\cdot\cdot}$, 530.1 eV), and oxygen in the lattice (O_O^X, 528.0 eV) [1-3]. The oxygen-related defect peak is considered an oxygen vacancy because it is the dominant defect in perovskite oxides. Thus, the $[V_O^{\cdot\cdot}]/[O_O^X]$ intensity ratio was denoted as the oxygen vacancy concentration. The hydroxyl group rapidly disappeared after etching a few nanometers since the OH⁻ typically adsorbed at the surface of thin film electrodes.
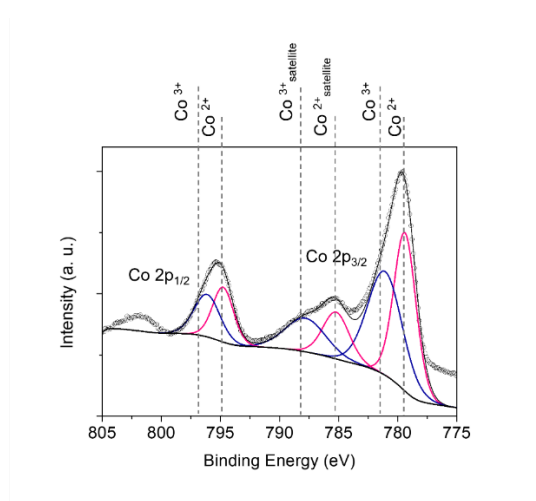
Figure S3. Fitting of the Co 2p photoelectron spectra.

The Co 2p photoelectron spectra were divided into two energy sets, Co $2p_{1/2}$ and Co $2p_{3/2}$, with an energy gap of approximately 15 eV [4, 5]. These spectra can be further deconvoluted into two oxidation states of Co^{2+} and Co^{3+}: Co^{2+} at the lower binding energy both in the main peak ($2p_{1/2}$ and $2p_{3/2}$ for 795 and 779 eV, respectively) and satellite peak (786 eV), and Co^{3+} at the higher binding energy both in the main peak ($2p_{1/2}$ and $2p_{3/2}$ for 797 and 782 eV, respectively) and satellite peak (788 eV) [4-6]. The $[Co^{2+}]/[Co^{3+}]$ relative ratio was determined by calculating the fitted area for each state.

Figure S4. Fitting of the Sr 3d photoelectron spectra.

Sr 3d photoelectron spectra were fitted into two energy sets of Sr $3d_{5/2}$ and Sr $3d_{3/2}$ with the energy separation of approximately 1.9 eV [4, 7]. eV, respectively Sr 3d photoelectron spectra can be deconvoluted into $Sr_{non-lattice}$ at the lower binding energies ($3d_{5/2}$ and $3d_{3/2}$ for 132.9 and 135.0 eV, respectively) and $Sr_{lattice}$ at the lower binding energies ($3d_{5/2}$ and $3d_{3/2}$ for 131.3 and 133.2 eV, respectively) [4, 8].
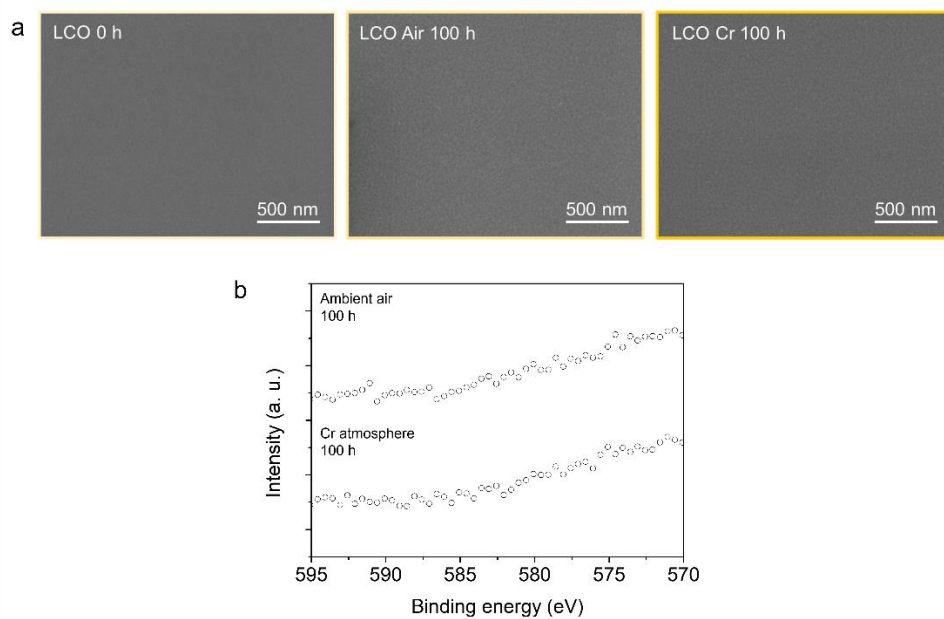
**Figure S5. Structural and chemical changes in the LCO electrode.** (a) SEM images of the LCO electrode before and after annealing at 600 °C for 100 h in ambient air and Cr atmosphere. (b) Cr 2p photoelectron spectra after annealing at 600 °C for 100 h in ambient air and Cr atmosphere.
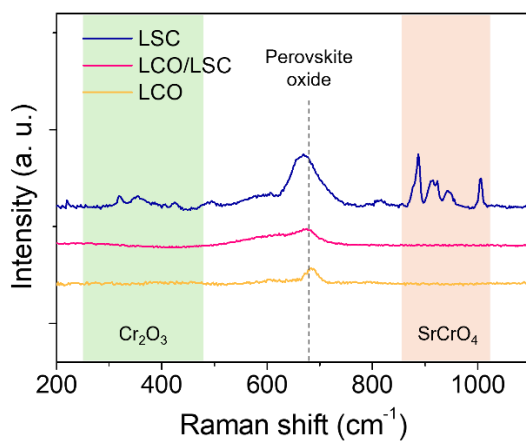
Figure S6. Raman spectra of the LSC, LCO/LSC, and LCO electrodes after annealing in Cr atmosphere for 100 h.
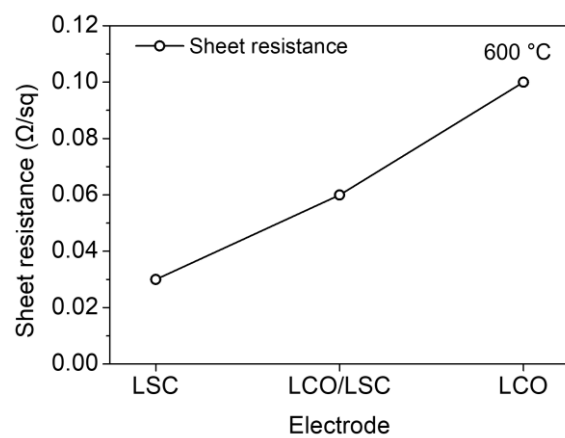
Figure S7. Sheet resistance of the LSC, LCO/LSC, and LCO model electrodes measured using a four-point probe.
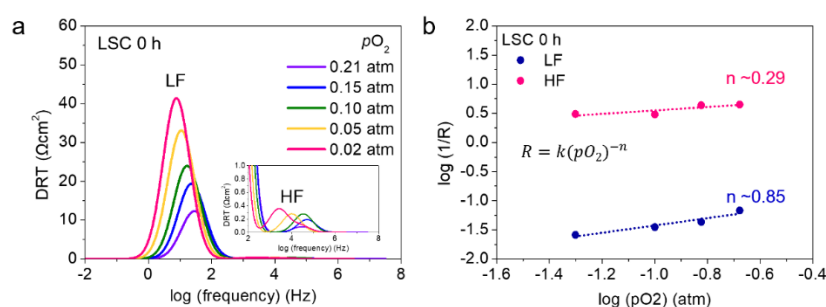
Figure S8. (a) DRT plot of the initial state of LSC electrode as a function of the frequency at different pO2 in the range of 0.02 to 0.21 atm. (b) R_p values of the initial state of the LSC electrode at R_{LF} and R_{HF} as a function of the oxygen partial pressure.

Table S1. Elementary ORR and reaction order

$O_{2\,(g)} \leftrightarrow O_{2,ad}$	1
$O_{2,ad} \leftrightarrow 2O_{ad}$	1/2
$O_{ad} + e^- \leftrightarrow O_{ad}^{2-}$	3/8
$O_{TPB} + 2e^- + V_O^{\cdot\cdot} \leftrightarrow O_O^X$	1/4

A DRT analysis was conducted to identify the peaks in the Bode plot. Figure S8(a) presents the overall plots and a magnified view of the high-frequency responses. Two distinct peaks were identified in the low-frequency (LF, 10^0-10^2 Hz) and high-frequency (HF; >10^2 Hz) ranges. To define the rate-determining step in each frequency range, the R_{LF} and R_{HF} of the LSC electrode were measured at controlled oxygen partial pressures in the range of 0.02 to 0.21 atm. Figure S8(b) shows that the change in R_p is proportional to oxygen partial pressure ($R_p \propto 1/p\,(O_2)^n$) [9]. The value of n can be used to identify specific reaction steps in the overall electrochemical reaction (Table S1). The R_{LF} and R_{HF} were measured to be 0.85 and 0.29, representing the oxygen diffusion and adsorption, and charge transfer reactions, respectively.
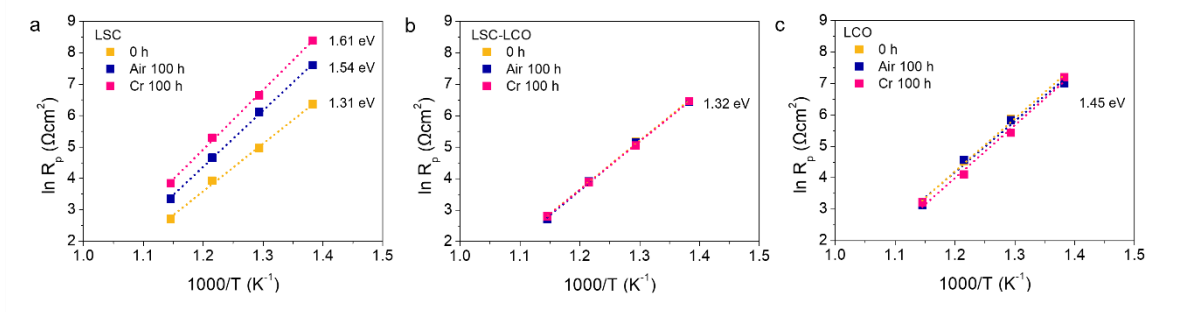
Figure S9. Arrhenius plots at the initial state after the stability test for 100 h in ambient air, and in Cr atmosphere. (a) LSC, (b) LCO/LSC, and (c) LCO electrodes.
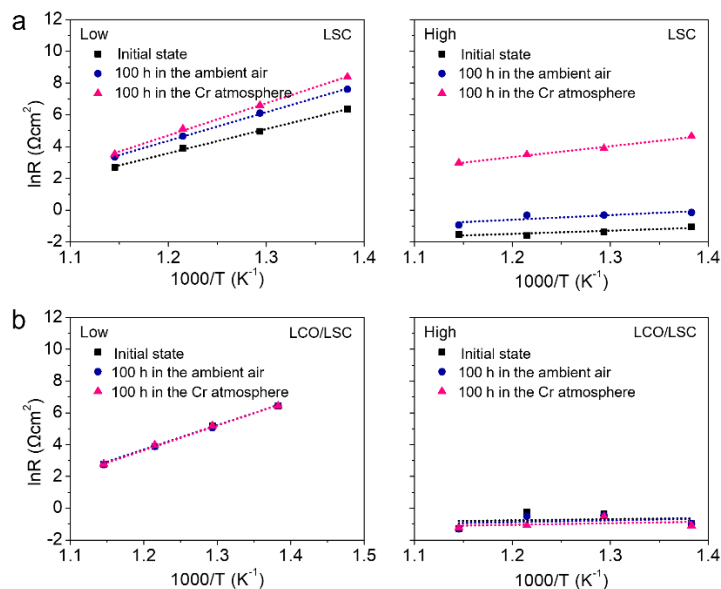
**Figure S10. Comparison of total activation energies.** Arrhenius plots for total polarization resistance of (a) LSC, (b) LCO/LSC, and (c) LCO at initial state, 100 h after stability test in ambient air and Cr atmosphere.

We compared the Arrhenius plots before and after the stability tests. Figure S9 shows the increase in the activation energy for the total R_p of the LSC electrode at 100 h in ambient air (1.54 eV) and at 100

h in the Cr atmosphere (1.61 eV) compared to its initial state (1.31 eV). This increase in the activation energy indicates a substantial change in the ORR kinetics. Figure S9 shows the changes in the activation energy resulting from the increase in the activation energies of both R_{LF} and R_{HF}. In particular, the activation energy of R_{LF} increased from 1.32 eV at its initial state to 1.55 eV at 100 h in the ambient air and 1.76 eV at 100 h in the Cr atmosphere. This increase can be attributed to a significant decrease in the reactivity for gas diffusion and adsorption owing to excessive Sr segregation and the formation of secondary phases, resulting in a nonstoichiometric surface [10]. Similarly, the activation energy of R_{HF} increased from 0.13 eV at its initial state to 0.25 eV at 100 h in the ambient air and 0.57 eV at 100 h in Cr atmosphere, indicating a significant decrease in reactivity for charge transfer reactions in the LSC bulk. The more significant changes in the activation energies of both the R_{LF} and R_{HF} in the Cr atmosphere can be attributed to the formation of additional Cr-induced secondary phases at the LSC surface and in the bulk, respectively.
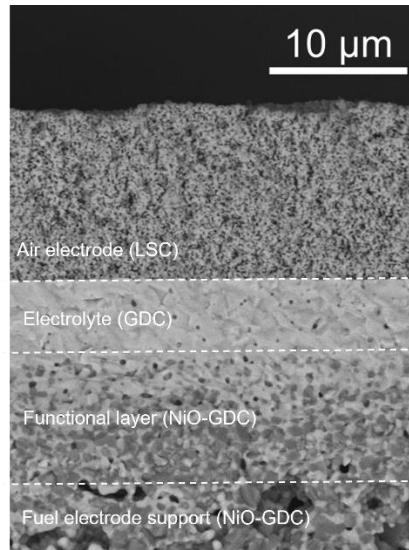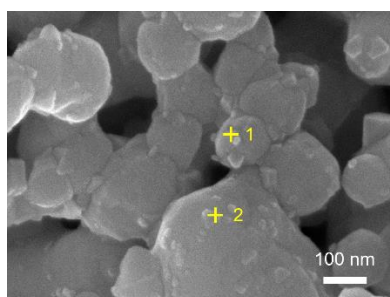
Figure S11. Cross-sectional SEM image of a single cell supported by a Ni-GDC-based anode.
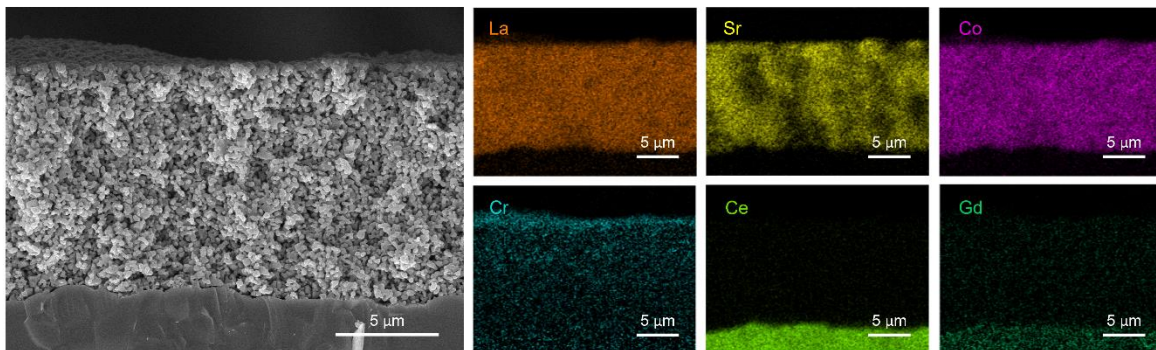
Figure S12. EDX mapping of the LSC electrode in a single cell configuration.
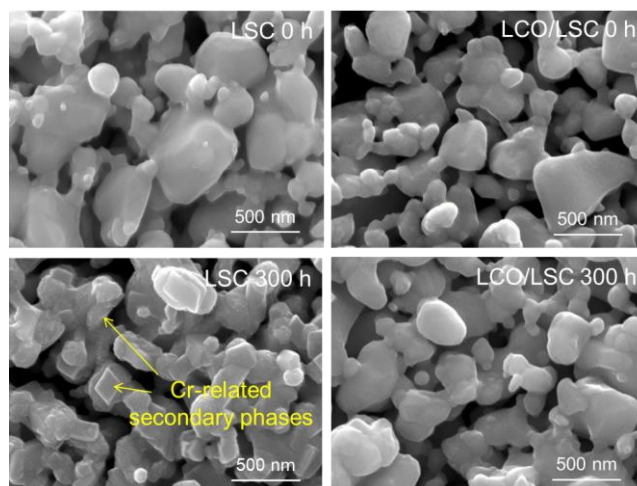
Figure S13. SEM images of the LSC and LCO/LSC electrode before and after the stability test at 600 °C for 300 h in Cr atmosphere.

Figure S14. SEM-EDX point image of the LSC electrode after stability test at 600 °C for 300 h in Cr atmosphere.

Table S2. Atomic ratios of the LSC electrode derived from EDX after the stability test at 600 °C for 300 h in Cr atmosphere.

spectrum	At %			
	La	Sr	Co	Cr
1	28.07	20.36	43.28	8.28
2	26.58	21.08	43.18	9.15
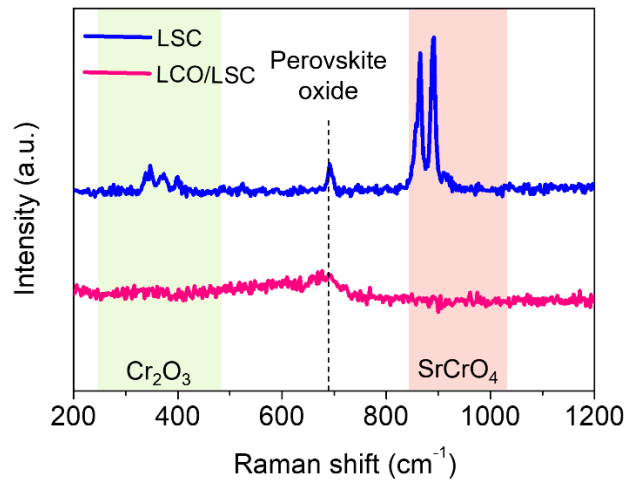
Figure S15. Raman spectra of the LSC and LCO/LSC cells after the stability test at 600 ℃ for 300 h in Cr atmosphere.

References

1. K. K. Banger, Y. Yamashita, K. Mori, R. L. Peterson, T. Leedham, J. Rickard and H. Sirringhaus, *Nat. Mater.*, 2011, **10**, 45-50.

2. S. A. Lee, S. Oh, J.-Y. Hwang, M. Choi, C. Youn, J. W. Kim, S. H. Chang, S. Woo, J.-S. Bae, S. Park, Y.-M. Kim, S. Lee, T. Choi, S. W. Kim and W. S. Choi, *Energy Environ. Sci.*, 2017, **10**, 924-930.

3. F. Lei, Y. Sun, K. Liu, S. Gao, L. Liang, B. Pan and Y. Xie, *J. Am. Chem. Soc.*, 2014, **136**, 6826-6829.

4. J.F. Moulder, W.F. Stickle, P.E. Sobol and K.D. Bomben, *Handbook of X-ray Photoelectron Spectroscopy*, Perkin-Elmer Corporation, United States of America, 1992.

5. Y. Zhu, L. Zhang, B. Zhao, H. Chen, X. Liu, R. Zhao, X. Wang, J. Liu, Y. Chen and M. Liu, *Adv. Funct. Mater.*, 2019, **29**.

6. M. Choi and W. Lee, *Chem. Eng. J.*, 2022, **431**.

7. H. G. Seo, H. Kim, W. Jung and H. L. Tuller, *Appl. Catal. B-Environ.*, 2024, **355**.

8. M. Siebenhofer, C. Riedl, A. Nenning, W. Artner, C. Rameshan, A. K. Opitz, J. Fleig and M. Kubicek, *J. Mater. Chem. A*, 2023, **11**, 12827-12836.

9. J. Lee, S. Hwang, M. Ahn, M. Choi, S. Han, D. Byun and W. Lee, *J. Mater. Chem. A*, 2019, **7**, 21120-21127.

10. W. Lee, J. W. Han, Y. Chen, Z. Cai and B. Yildiz, *J. Am. Chem. Soc.*, 2013, **135**, 7909-7925.